Step-Stare Image Gathering for High-Resolution Targeting

Valérie Lavigne, Benoit Ricard
Defence R&D Canada – Valcartier
2459 Pie-XI Blvd North, Val-Bélair
Québec, Canada

{valerie.lavigne.aerex or benoit.ricard}@drdc-rddc.gc.ca

ABSTRACT

Built around two infrared cameras and a high-speed opto-mechanical pointing mechanism, the Infrared Eye attempts to mimic the human eye by superimposing a high-resolution narrow field of view (first camera) for target identification over a lower resolution wide field of view (second camera) for situation awareness. A high-performance opto-mechanical pointing system allows the narrow field to be positioned anywhere within the wider field providing the operator with fast access to points of interest without losing situation awareness.

During the development of the Infrared Eye, we found that we could use the opto-mechanical pointing system to produce high-resolution, wide field of view images at very high speed. The pointing system rapidly moves the narrow field of view to take high-resolution images that can then be assembled into a mosaic in a dynamic fashion, taking into account the movements of the platform to optimize the selection of mosaic sub-images. By using the high-resolution narrow field images to fill the mosaic, a wide field of view can be covered with the same high resolution as the conventional narrow field images.

As compared to the current Infrared Eye concept, the step-stare approach eliminates one of the two cameras for a lighter and more compact system, while increasing the resolution in the wide field of view coverage, which would be impossible using conventional cameras and optics as wide field and high resolution are mutually opposed trade-off parameters in an optical design. The wide field and high resolution obtained by the step-stare technique also brings the detection capability in the wide field to the same level as that obtained with a narrow field camera in a conventional FLIR system. Within its related R&D activities, DRDC Valcartier has demonstrated the possibility to fabricating wideband Risley prisms in both the MWIR and LWIR spectra, as well as narrower band prisms in the visible and near IR spectra for passive and active imaging. The applications considered are UAV surveillance platforms for peacekeeping and tactical information acquisition, sensor packages for other manned airborne platforms or land-based perimeter surveillance. The capacity of the Risley prisms to point the field of view of the camera anywhere within its design coverage (> 50°) allows one to configure the vertical and horizontal dimensions of the mosaic image according to the requirements of the mission. A miniature prism package is also under design and will be fitted in front of small low-cost, low-power micro IR imagers of the 160x120 pixels class. This combination could provide mini UAVs with a high-resolution IR payload under 3 Kg.

In this paper, we will describe the opto-mechanical pointing system used for the step-staring system and its different variations. We will also describe the image acquisition and control algorithms developed to build the mosaic dynamically by taking into account the attitude and position of the airborne platform. A simulator has been developed and will be demonstrated to show how it is used to validate our image acquisition scenario. Finally, imagery from our step-stare system will be presented and discussed.

Lavigne, V.; Ricard, B. (2005) Step-Stare Image Gathering for High-Resolution Targeting. In *Advanced Sensory Payloads for UAV* (pp. 17-1 – 17-14). Meeting Proceedings RTO-MP-SET-092, Paper 17. Neuilly-sur-Seine, France: RTO. Available from: http://www.rto.nato.int/abstracts.asp.

Report Documentation Page

Form Approved
OMB No. 0704-0188

1. REPORT DATE	2. REPORT TYPE	3. DATES COVERED
01 MAY 2005	**N/A**	**-**

4. TITLE AND SUBTITLE	5a. CONTRACT NUMBER
Step-Stare Image Gathering for High-Resolution Targeting	5b. GRANT NUMBER
	5c. PROGRAM ELEMENT NUMBER
6. AUTHOR(S)	5d. PROJECT NUMBER
	5e. TASK NUMBER
	5f. WORK UNIT NUMBER
7. PERFORMING ORGANIZATION NAME(S) AND ADDRESS(ES) **Defence R&D Canada Valcartier 2459 Pie-XI Blvd North, Val-Bélair Québec, Canada**	8. PERFORMING ORGANIZATION REPORT NUMBER
9. SPONSORING/MONITORING AGENCY NAME(S) AND ADDRESS(ES)	10. SPONSOR/MONITOR'S ACRONYM(S)
	11. SPONSOR/MONITOR'S REPORT NUMBER(S)

12. DISTRIBUTION/AVAILABILITY STATEMENT
Approved for public release, distribution unlimited

13. SUPPLEMENTARY NOTES
See also ADM202032., The original document contains color images.

14. ABSTRACT

15. SUBJECT TERMS

16. SECURITY CLASSIFICATION OF:			17. LIMITATION OF ABSTRACT	18. NUMBER OF PAGES	19a. NAME OF RESPONSIBLE PERSON
a. REPORT	b. ABSTRACT	c. THIS PAGE			
unclassified	**unclassified**	**unclassified**	**UU**	**14**	

Standard Form 298 (Rev. 8-98)
Prescribed by ANSI Std Z39-18

1.0 INTRODUCTION

With a changing climate and varied terrain of a 15,540,000 square kilometres surface (Canada's landmass, territorial waters and mid-ocean sections of the Atlantic and Pacific), search and rescue and surveillance operations are a great challenge in Canada. These operations are often carried out at night or under other conditions of poor visibility such as smoke, fog or snow. Many difficulties in surveillance material conception for those operations arise from the operational context of the missions. The most significant requirement for the system is its capacity to allow the detection and the identification of the object of interest. Detection requires a wide field of view, whereas identification requires a high resolution. This presents a great challenge because these concepts are opposed and it is generally necessary to reach an agreement between the two. One of the solutions usually proposed to solve the resolution versus field of view dilemma is to alternate between two selectable fields: a low resolution wide field and a high resolution narrow field at the cost of loosing situation awareness when operating in narrow field of view (NFOV) and the identification capability when using the wide field of view.

An innovative approach was developed with the Infrared Eye project [1, 2] at Defence R&D Canada Valcartier. It tries to imitate the human eye by superimposing a high-resolution narrow field of view for target identification over a low-resolution wide field of view for situation awareness. A high performance opto-mechanical pointing system allows the narrow field to be positioned anywhere within the wider field. The position of the narrow field follows the line of sigh of the operator provided by an eye-tracking system. Over the years, it became obvious to the team that the narrow field of view opto-mechanical pointing system could be used alone, without the wide field of view camera to produce a large and high-resolution mosaic image.

In this paper, we will describe the opto-mechanical pointing system used for the step-staring system and its different variations. We will also describe the mathematical model and control algorithms used to build the mosaic dynamically from multiple images by taking into account the attitude and position of the airborne platform. Moreover, to validate the step-stare system operations and the effectiveness of the algorithms, a simulator has been developed and will be presented. This paper will conclude by presenting preliminary results from the first prototype of a high-speed step-stare system and discussion of its usage in unmanned platform.

2.0 STEP-STARE CONCEPT

The step-stare concept is quite simple. Using the pointing system based on a pair of achromatic Risley's prisms that were developed for the Infrared Eye, the step-stare technique rapidly builds a high-resolution, large area coverage mosaic from the smaller images. Building a mosaic in a dynamic context brings out many challenges not present in a static context. Being on an airborne platform, the point of view of the camera is changing constantly, and at a given time instant, images that were previously taken must be warped to be correctly displayed with that taken from the current point of view. A dynamic strategy that adapts automatically to the operational context was developed to control image acquisition according to criteria based on the state of the mosaic. The images taken are geo-referenced by the projection of their corner onto the ground using flight data. They are assembled according to the actual point of view with homographic transformations.

The methods used for display corrections due to the airborne platform displacement are explained in section 4.1. Also, since the narrow field of view can be positioned anywhere within the wide field coverage, we need a strategy to select the position where to take the next image. Our dynamic acquisition strategy is described in section 4.2. The model used to map pixels to geo-referenced positions and vice-versa is detailed in section 3. We also developed a software simulator to optimize and test our algorithms. This simulator and some simulation results are presented in section 5. Section 6 shows the prototype that

implements the step-stare strategy and includes a few results from real experimentation. More details about the model, the strategy and the simulation are given in Refs. 3 and 4.

3.0 SYSTEM MODEL

We have modelled the acquisition system in order to establish the correspondence between ground coordinates and mosaic pixels. Therefore the model deals mostly with projections and positioning. The main components of the model are a set of prisms, a camera and an airborne platform.

Two right-handed Cartesian 3D coordinate systems are used with the model: the camera referential C and the world referential W. Two 2D referentials I and M are used to represent pixel coordinates in the camera image and the mosaic planes respectively. An overview of the coordinate systems is shown in Fig. 1.

The Risley prisms are both aligned on the optical axis of the camera. The pointing system setting is described in Ref. 3. Each prism produces a deviation of the optical axis that moves the narrow field image centre away from the mosaic image centre. When the two prisms are opposed, there is no deviation at all and when they are aligned, the deviation is maximal. The prisms can rotate and the two deviations are summed up vectorially. In our model, we represent the total deviation with its horizontal component θ_h and its vertical component θ_v. In Fig. 2, θ_h has a positive value and θ_v has a negative value.

The camera model used in this paper is the standard pinhole model, which performs a linear projective mapping of the 3D world into the image frame. The camera will be fixed under the airborne platform using a stabilized pan and tilt mount. The optical axis of the camera is oriented along the x_c axis and the z_c axis points towards the top of the camera. The position and altitude of the camera is (pos_x, pos_y, alt) relative to W. The C and W frame referentials can be aligned using a *Roll-Pitch-Yaw* rotation. The roll angle γ turns around x_c, the pitch angle β rotates around y_c and the yaw angle α makes the last rotation around z_c. These angles and their direction of rotation (using the right hand rule) are shown in Fig. 1.

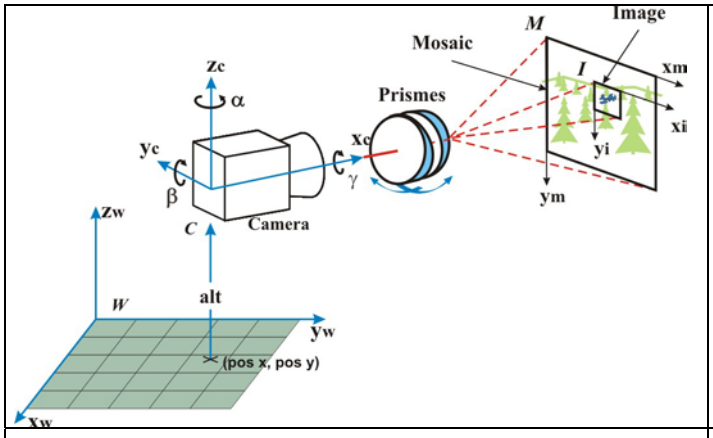

Figure 1: System referentials.

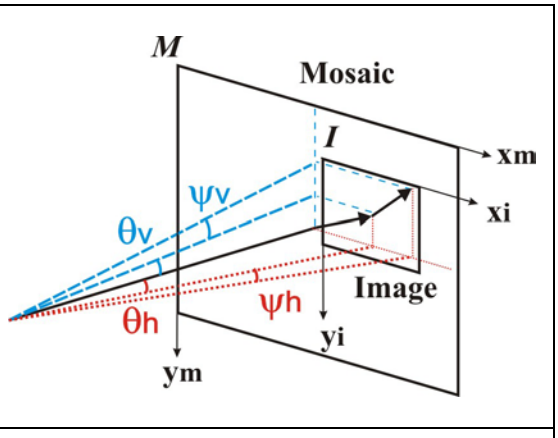

Figure 2: Prism angles.

Rotation matrices are used to convert positions from one referential to another. Equation (1) is used to find the (x_w, y_w, z_w) coordinates in the world referential W of the point (x_c, y_c, z_c) in C. The reverse conversion is achieved by first subtracting (pos_x, pos_y, alt) from (x_w, y_w, z_w) and then applying the rotation matrices in reverse order with negative angles.

3.1 Ground Projection

If we know its horizontal ψ_h and vertical ψ_v angles relative to the image centre, we can find the projection on the ground of any image pixel. These angles are shown in Figure 2. For the image corners, $\psi_h = \pm fov_{ih}/2$ and $\psi_v = \pm fov_{iv}/2$, where fov_{ih} and fov_{iv} are the horizontal and vertical fields of view of the narrow field camera image.

$$\begin{bmatrix} pos_x \\ pos_y \\ alt \end{bmatrix} + \underbrace{\begin{bmatrix} \cos\alpha & -\sin\alpha & 0 \\ \sin\alpha & \cos\alpha & 0 \\ 0 & 0 & 1 \end{bmatrix}}_{R_\alpha} \underbrace{\begin{bmatrix} \cos\beta & 0 & \sin\beta \\ 0 & 1 & 0 \\ -\sin\beta & 0 & \cos\beta \end{bmatrix}}_{R_\beta} \underbrace{\begin{bmatrix} 1 & 0 & 0 \\ 0 & \cos\gamma & -\sin\gamma \\ 0 & \sin\gamma & \cos\gamma \end{bmatrix}}_{R_\gamma} \begin{bmatrix} x_c \\ y_c \\ z_c \end{bmatrix} \quad (1)$$

For the projection, we need a unit vector pointing in the direction of the ground coordinates mapped by the pixel. We first build a vector in C pointing towards the desired pixel of the mosaic from a unit vector oriented towards the optical axis (x_c). Two rotations are needed: a rotation of an angle $\varphi_h = -\psi_h - \theta_h$ around z_c and a rotation around y_c of an angle $\varphi_v = \psi_v + \theta_v$. Then, by applying the camera-to-world rotation matrices from Eq. (1), we obtain the unit length projection vector (x_p, y_p, z_p) along W axes but relative to C origin. Equation (2) combines these two operations.

$$\begin{bmatrix} x_p \\ y_p \\ z_p \end{bmatrix} = R_\alpha R_\beta R_\gamma \cdot \underbrace{\begin{bmatrix} \cos(\phi_h) & -\sin(\phi_h) & 0 \\ \sin(\phi_h) & \cos(\phi_h) & 0 \\ 0 & 0 & 1 \end{bmatrix}}_{R_{\phi_h}} \underbrace{\begin{bmatrix} \cos(\phi_v) & 0 & \sin(\phi_v) \\ 0 & 1 & 0 \\ -\sin(\phi_v) & 0 & \cos(\phi_v) \end{bmatrix}}_{R_{\phi_v}} \cdot \begin{bmatrix} 1 \\ 0 \\ 0 \end{bmatrix} \quad (2)$$

For the next equation, we suppose that the ground is flat. Thus we need to find the intersection of the projection vector with the x_w - y_w plane. We stretch it until its z_p component is the same length as the aircraft's altitude alt, but negative. The only step left is the translation from the origin of coordinate system C to W. This result is given by Equation (3).

$$\begin{bmatrix} x_w \\ y_w \\ 0 \end{bmatrix} = \left(\begin{bmatrix} x_p \\ y_p \\ z_p \end{bmatrix} \cdot \frac{(-alt)}{z_p} \right) + \begin{bmatrix} pos_x \\ pos_y \\ alt \end{bmatrix} \quad (3)$$

The flat ground hypothesis is a good approximation if the aircraft flies over the sea or at high enough altitude over slightly uneven land. Only Equation (3) depends on it. In a situation where the scene cannot be represented by a plane, a 3D model such as an elevation map (like DTED) could be used in order to determine the intersection of a specific projection vector with the scene content.

3.2 Horizon Limitation

However, Equation (3) does not apply when the projection reaches the ground too far or points above the horizon. We use the visible horizon distance $r_{dist} = 3924.31\sqrt{alt}$ (meters), as defined in Ref. 5 for this specific case. If the inequality of Equation (4) is not respected, we do not attempt to find the ground coordinates because it means that the projection vector will not reach the ground within the horizon limit. Instead, we will rather find its intersection with a half-sphere of r_{dist} radius whose centre is the (pos_x, pos_y) position on the ground under the aircraft. We stretch the vector (x_p, y_p, z_p) by a factor f to reach the half-sphere. This intersection position will be represented using the spherical coordinate system shown in Fig. 3. Eqs. (5) and (6) are used to find the spherical coordinates of the intersection.

$$\frac{-alt}{z_p} \geq \frac{\sqrt{x_p^2 + y_p^2}}{r_{dist}} \quad (4)$$

$$(fx_p)^2 + (fy_p)^2 + (fz_p + alt)^2 = r_{dist}^2,$$

$$\text{so} \quad f = -z_p \cdot alt + \sqrt{(z_p \cdot alt)^2 - alt^2 + r_{dist}^2} \quad (5)$$

$$\theta = \arctan(\frac{y_p}{x_p}) \quad \text{and} \quad \phi = \arccos(\frac{fz_p}{r_{dist}}) \quad (6)$$

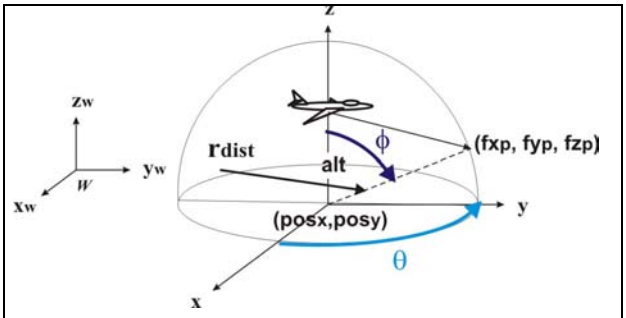

Figure 3: Spherical coordinate system.

Centring the half-sphere on the aircraft position means that these intersection points will travel according to the aircraft displacement. This describes what would happen with an object point located at an infinite distance. Although it is not perfectly accurate, this is not a bad approximation because image points that map the sky and objects around the horizon line can usually be considered very far. With Equation (7) we can find back the Cartesian coordinates in the *W* referential.

$$x_w = r_{dist}\cos(\theta)\sin(\phi) + pos_x, \quad y_w = r_{dist}\sin(\theta)\sin(\phi) + pos_y \quad \text{and} \quad z_w = r_{dist}\cos(\phi) \quad (7)$$

3.3 Reverse Projection

For display purposes, we also need to find the φ_h and φ_v angles relative to the mosaic centre from the coordinates (x_w, y_w, z_w) in frame referential *W*. After reversing the translation between *W* and *C*, using Equation (8), we normalize the vector to undo the stretching. Then, we make the reverse rotations of Eq. (1), which gives the (x_c, y_c, z_c) vector in *C*. We know that if we could also revert the $R\varphi_h$ and $R\varphi_v$ rotations of Equation (2), we would get back the unit vector along x_c. This leads to the equality of Equation (9), which is solved by Equation (10). The $cos(\varphi_v)$ terms in Equation (10) are not simplified because they allow us to find the correct quadrant angle.

$$\begin{bmatrix} x_c \\ y_c \\ z_c \end{bmatrix} = R_{-\gamma}R_{-\beta}R_{-\alpha} \cdot \left(\begin{bmatrix} x_w \\ y_w \\ z_w \end{bmatrix} - \begin{bmatrix} pos_x \\ pos_y \\ alt \end{bmatrix} \right) / \left\| \begin{bmatrix} x_w \\ y_w \\ z_w \end{bmatrix} - \begin{bmatrix} pos_x \\ pos_y \\ alt \end{bmatrix} \right\| \quad (8)$$

$$\begin{bmatrix} x_c \\ y_c \\ z_c \end{bmatrix} = \begin{bmatrix} \cos(\phi_h)\cos(\phi_v) \\ \sin(\phi_h)\cos(\phi_v) \\ -\sin(\phi_v) \end{bmatrix} = R_{\phi_h}R_{\phi_v} \cdot \begin{bmatrix} 1 \\ 0 \\ 0 \end{bmatrix} \quad (9)$$

$$\phi_v = -\arcsin(z_c) \quad \text{and} \quad \phi_h = \arctan\left(\frac{y_c/\cos(\phi_v)}{x_c/\cos(\phi_v)}\right) \quad (10)$$

Now that we have φ_h and φ_v, Equation (11) gives the (x_m, y_m) pixel position of the object in the mosaic referential *M*. We use the fact that the horizontal and vertical fields of view covered by the mosaic, fov_{mh} and fov_{mv}, and their corresponding mosaic width w_m and height h_m in pixels are known. As usual, the top left corner of the mosaic image is the origin of the coordinate system.

$$x_m = \frac{w_m}{2}\left(1 + \frac{\tan(-\phi_h)}{\tan(fov_{mh}/2)}\right) \quad \text{and} \quad y_m = \frac{h_m}{2}\left(1 + \frac{\tan(\phi_v)}{\tan(fov_{mv}/2)}\right) \quad (11)$$

4.0 STEP-STARE STRATEGY

As explained in section 2, the step-stare strategy requires building a mosaic from the images already taken and selecting the narrow field position from which the next image will be taken. More specifically, after the initialization step, the operations of the step-stare approach are: take an image, build the mosaic from the images we have, erase the obsolete ones, evaluate the next position, move the prisms to that position and start over again.

4.1 Mosaic Display

The mosaic we generate is constructed with images that were all taken from different locations and orientations. Thus, we need a reference to locate the image position in the real world. We chose to use the projection of the four image corners on the ground or on the half-sphere as references. These positions are recorded with each image and can be computed using the equations presented in sections 3.1 and 3.2. For these reference points, we can find their pixel position in the mosaic for the current point of view, by using the reverse projection equations of section 3.3. However, we cannot copy the image directly in the mosaic, because its area within the mosaic is generally not a rectangle due to prisms distortions and changing point of view. This is especially true when the aircraft is turning. This situation is depicted in Fig. 4, where w_i and h_i are the image width and height in pixels.

$$\begin{bmatrix} m \cdot x \\ m \cdot y \\ m \end{bmatrix} = \begin{bmatrix} a & b & c \\ d & e & f \\ g & h & 1 \end{bmatrix} \begin{bmatrix} u \\ v \\ 1 \end{bmatrix} \quad (12)$$

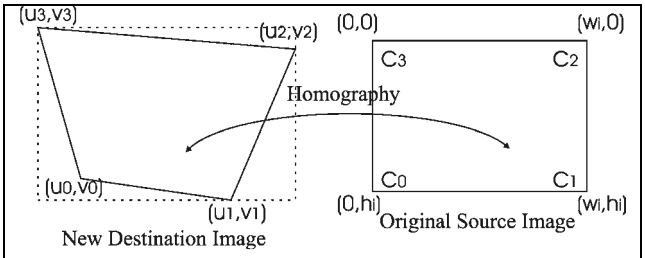

Figure 4: Image destination mapping.

To warp the images into the mosaic, we use a homography that associates each (u, v) destination pixel to a (x_i, y_i) source image pixel. The homography matrix is defined in Equation (12). We can write a system of eight equations using the eight source image corners coordinates and their associated destination coordinates. Solving this system will give us the eight unknown matrix values. The equations are simplified by the fact that half of the source image corners coordinates are zero. Thus, we can resolve the homography equation system analytically and avoid the computation of a matrix inversion for each image.

Since the transformation is known, the information about which area an image covers exactly is available. We can take advantage of the mapping step to compute statistics that will be useful through the rest of the algorithm. To keep track of the mosaic coverage, we use a pixel map. It is a matrix that is filled with the number of the image that covers each pixel. The pixel map is ten times smaller than the actual mosaic plus a half-image wide border whose use will be explained in section 4.2. After building the mosaic, we know the area in pixels an individual image covers. If the image does not cover enough pixels, it can be deleted from the bank of images and the pixel map is updated accordingly. The image management is done after the mosaic-building step but before the next position evaluation. It allows anticipating the creation of a hole in the mosaic (a set of pixels in the mosaic that do not map to any images) before it actually appears on the mosaic. The pixel map also makes it possible to know which areas need to be refreshed and the hole locations.

4.2 Acquisition Strategy

Although the mosaic is now ready to be displayed on the operator's console, we still have to decide where the next image will be taken. The order in which the images are collected is significant because of the aircraft motion. Using a set of fixed patterns requires that we define every possible situation and make sure that an image-taking pattern responds appropriately to it. The advantage of a dynamic acquisition strategy is that it adapts automatically to the operational context. The aim of the acquisition strategy is to make sure that each pixel of the mosaic is covered and that the refresh rate is as high as possible. Thus, the strategy is dependent on the mosaic state only. The coverage and image age information was stored in the pixel map through the previous algorithm steps, so we can use it to evaluate the mosaic situation.

The space that the maximum prism deviation angle may reach forms a circle whose radius is greater or equal to the distance between the mosaic centre and a corner image centre. The centre of an image could be positioned on any pixel within this circle. However, an evaluation of all of these positions would require a significant amount of computations to determine the best pixel on which to centre the next image. In order to reduce computation time, position selection is restricted to a limited set of fixed positions. These positions are laid in a grid whose size is selectable. The mosaic size can be smaller than the space covered by the prisms. The positions aligned with the grid on the mosaic sides and corners are added to the available step-stare positions if the prisms can reach them. These positions are called *outside* positions while the *inside* positions are those on the grid inside the mosaic (Fig. 5).

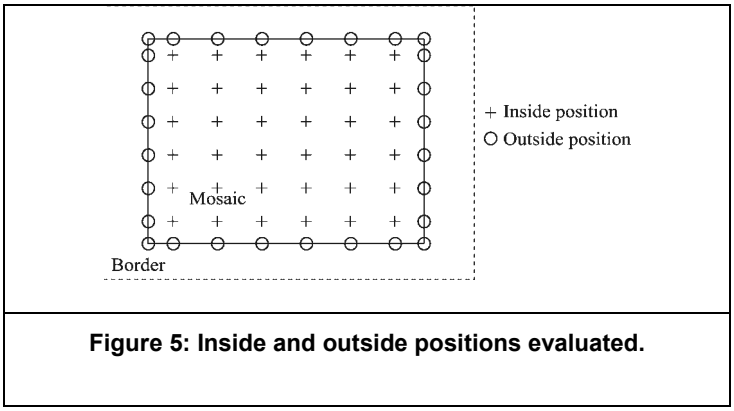

Figure 5: Inside and outside positions evaluated.

Since we use positions that are on the sides of the mosaic, this creates a half-image wide border around the mosaic that may also be filled with images (shown in dash lines in Fig. 5). This is why the pixel map is larger than the mosaic. When we take the border information into account, we can preventively fill the border with images. This avoids seeing holes moving into the mosaic due to the scrolling effect induced by aircraft motion.

All positions are evaluated using these three criteria: minimization of prism displacements, maximization of hole coverage and refresh rate. Each criterion is given a normalized value that ranges between 0 (less priority) and 1 (more priority). The total priority score is the weighted sum of the three criteria. The operator can adjust the weights. The position with the highest score is the position used to take the next image. To evaluate a given position, we use the information from a section of the pixel map that covers the area an image centred on this position would fill. Prism distortions are not considered for this step and this section is an image-size rectangle centred on the given position.

4.2.1 Prism Displacement

Minimization of the prisms' displacement time is desirable. If we spend less time moving the prisms, we can take more images and improve the mosaic refresh rate and quality.

The total deviation of the prisms can be represented on a plane with polar coordinates. To simplify the equations we select the plane parallel to the image plane for which the distance to the prisms is equal to 1. For a given (θ_h, θ_v) deviation, we can find its (ρ_t, ω) polar coordinates with Equation (13). As shown in Fig. 6, two vectors of equal length ρ are summed up to make the total deviation. Each of these vectors represents the projection on the plane of the deviation caused by the prism. The ρ length of the two vectors can be found using the maximum deviation angle θ_{max} the prisms can reach. With Equation (14), we obtain the value of θ_{max} and δ. The final prism angles are $\omega - \delta$ and $\omega + \delta$.

$$\rho_t = \sqrt{\tan(\theta_h)^2 + \tan(\theta_v)^2} \quad \text{and} \quad \omega = \arctan\left(\frac{\tan(\theta_v)}{\tan(\theta_h)}\right) \tag{13}$$

$$\rho = \frac{\tan(\theta_{max})}{2} \quad \text{and} \quad \delta = \arccos\left(\frac{\rho_t}{2\rho}\right) \tag{14}$$

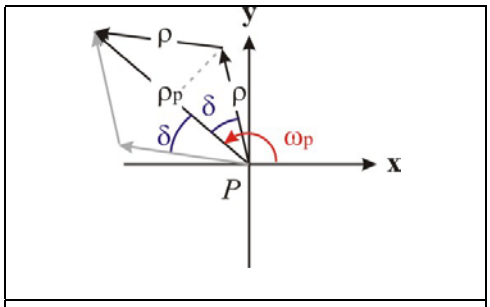

Figure 6: Individual prism angles.

We can find the prism angles corresponding to the next image centre position using the method just described. Because each of the two prisms can move to either of the two destination angles, there are two possible displacements. The total time of the displacement is dependent only on the prism with the greatest rotation angle. We find this angle for each possibility and then we keep the possibility for which the rotation angle is the smallest. The duration of the displacement is not linearly related to the angular distance *ang* travelled. To approximate this time, we suppose a constant positive acceleration *a* for the first half of the distance (*ang*/2) and an equal negative acceleration for the other half. Because $x/2 = 1/2 \cdot a(t/2)^2$, we know the displacement time is proportional to the square root of the angular distance *ang*. The final score for this criterion is given by $1 - \sqrt{ang/\pi}$. The π division normalizes the score and it is subtracted from one to give the highest priority to short prism displacements.

4.2.2 Hole Coverage

Hole presence in the mosaic is an important problem because there is always a slight chance the target was missed because it was located in a small unfilled area of the mosaic. The hole score for an image position is based on the percentage of its area that is not covered in the pixel map. We consider holes inside the mosaic to be more important than those on the border. However, filling the border will avoid hole apparition inside the mosaic. Therefore, if there are holes inside the mosaic, we consider holes on the border, but only if they represent more than 50% of the position area. To ensure that holes will obtain a significant score in comparison with the other criteria, a normalization factor that increases the priority of the largest hole of the mosaic to the maximum value is applied to the all resulting scores. However, this increase of hole importance means that a very high priority will also be granted to a tiny hole if it is the largest of the pixel map. To avoid this situation for border holes, we do not normalize the score if there are no holes inside the mosaic and all *outside* positions have at least 50% of their area covered.

4.2.3 Refresh Rate

Refreshing the mosaic rapidly and regularly makes it more accurate and improves detection. We define the age of an image as the number milliseconds that passed since the image was acquired. To evaluate the age of an *inside* position, we compute the age average of the pixels it contains. For *outside* positions, we also compute the average of the pixel ages. However, for pixels located on the border and in holes, their age is defined as the median age of the images still present in the mosaic. The true age of border pixels is not

used in the average because its content is not displayed on the screen and we are not interested in having a high refresh rate for it. Finally, the resulting scores are normalized to ensure that they all respect the [0, 1] range.

5.0 STEP-STARE SIMULATOR

We have implemented a complete simulator to test and develop our step-stare strategy. With the simulator, new algorithms can be implemented and tested rapidly. We can also use it to test ideas that would otherwise require expensive settings.

5.1 Interface

The interface of the simulator is shown in Fig. 7. It contains all the controls needed to enter the simulation parameters and command the simulation execution. Three images illustrate the state of the simulation. First, the platform view (top-left) shows the aircraft from above and the mosaic and camera image contours projected on the ground. The ground image used in the simulator is a large IR image mosaic that was built from real flight data. Next, the mosaic view (bottom-left) shows the result obtained with the step-stare algorithm. Optional frames around the camera images can be added to help distinguish the image positions. Finally, the algorithm view (bottom-right) shows the state of the pixel map, including the border, where the newest pixels are displayed with a bright red and holes are black. Figure 8 shows the interface of the trajectory generator included in the simulator. It allows fast aircraft trajectory creation with the camera pointing to a specified direction relative to the aircraft or constantly adapting its orientation to stare at a target on the ground.

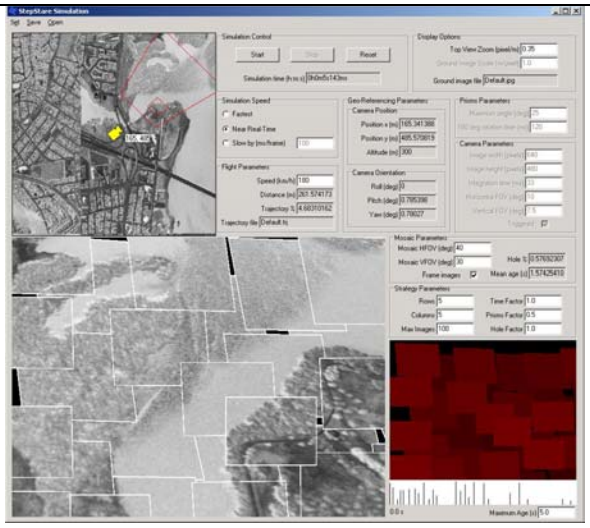

Figure 7: Step-stare simulator interface.

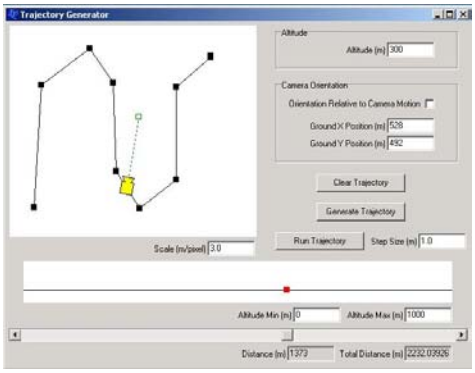

Figure 8: Trajectory generator.

5.2 Simulation Results

The frames around the images of the mosaics presented would not normally be displayed on an operator console. They are added to the images in order to highlight where they are inserted in the mosaic for analysis purposes. Figure 9 presents the order in which the first images are taken with a 5 by 5 image positions grid when the aircraft is flying straight. A pattern of this kind always appears in the beginning of the algorithm since two of the criteria favour the rapid covering of the mosaic. After that, if the aircraft continues to fly straight with a constant speed, the acquisition pattern changes and becomes stable. It will

mostly select images on the sides that are scrolling away and regularly refresh some other position within the mosaic when they become outdated. When the aircraft turns, the acquisition strategy will once again adapt and try to fill the positions where holes appear from the side. Figure 10 shows the importance of image warping when the aircraft is turning.

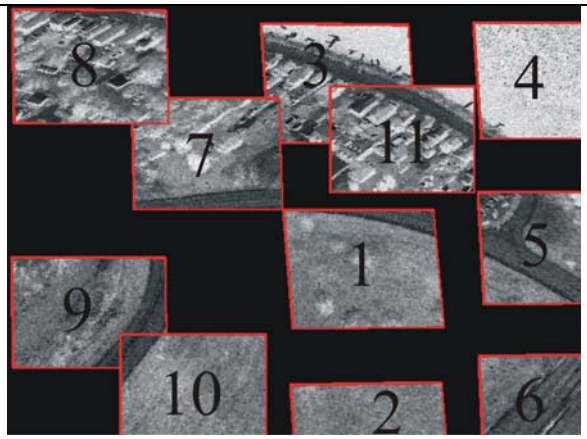

Figure 9: Straight flight mosaic.

Figure 10: Mosaic during a turn.

6.0 SYSTEM DESCRIPTION

In the last sections, it has been demonstrated that it is possible to make a high-speed, high-resolution, large field of view infrared images by using Risley's prisms and a simulator proved the efficiency of the algorithms used. As in any engineering systems, it is only when the "rubber hits the road" that you know if it will work effectively. To validate the effectiveness of our system, a prototype based on the concept of the Infrared Eye opto-mechanical pointing device has been built. Over the last few months, experiments have been conducted to quantify and to improve the pointing accuracy of the prism device. In the next sections, a description of hardware, software and the calibration process will be presented.

6.1 Hardware Description

The step-stare system is composed of: a Indigo's Phoenix LWIR camera (8µm-9.2µm, snapshot integration, 640x512, digital output), a 100 mm Risley's prisms, driven by 2 – 150 W Maxon brushless motor, a 1 axis fibre-optic gyro coupled with a 2-axes tilt sensor and an acquisition computer (Figure 11). The tilt sensor and fibre-optic gyro are used together to provide precise reading of rotation on the azimuth axis where the tilting induced inaccuracy is compensated by the tilt sensor. It is worth mentioning that, in the current test phase, the step-stare camera head is kept stationary (no translation); we only induce rotation to the platform.

The mosaic creation needs a tight synchronisation between the components of the system. First, the acquisition computer (AC) computes the next best view as defined in section 4.2 and sends a command to the motor drivers. When they reach their commanded positions, the AC takes a new frame from the camera. At the completion of the camera integration time, the AC acquires the actual position and attitude of the camera and computes a new position for the prisms. During the prisms displacement, the AC processes the acquired images, as described in section 4.1 and sends them to the operator station.

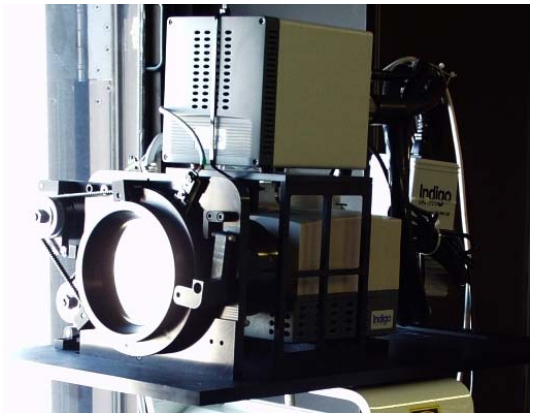

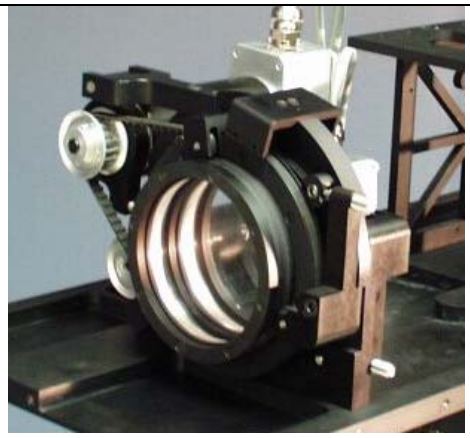

Figure 11: Prototype of the step-stare system. Complete system with the Phoenix camera (left) and the opto-mechanical pointing device (right).

6.2 Software Description

The step-stare control program interface is similar to the simulator. They both use the same version of the strategy. All hardware drivers have been wrapped with COM interfaces. The control program is set up from XML files and creates the drivers objects dynamically using this configuration information. It means that, as long as its drivers implement the appropriate interface, a hardware system can be replaced with another without recompiling the application. Only the configuration file has to be updated. Simulated hardware drivers have been developed for the simulator. In our implementation of the strategy, Direct3D from Microsoft carries out the warping of source images to their destination in the mosaic according to the homography matrix in real-time (section 4.1). Image acquisition and prisms displacement commands are issued asynchronously in order to optimize code execution.

6.3 Prism Deviation Calibration

In order to accurately aim the NFOW using the Risley's prism, a procedure has been developed to establish a relation between angular position of the prisms and the resulting NFOV deviation angles in elevation and azimuth. As seen in Figure 12, aiming of the NFOV is caused by the vectorial sum of both prisms deviation. Actually, the resulting deviation could be decomposed in two types of prism motions: motions of the prisms in which their relative angular separation changes (i.e. they turn in opposite directions) and prism motions in which their relative angular separation stay constant (i.e. they turn at the same speed). This behaviour is the basis of the prism deviation calibration strategy. For the purpose, the step-stare camera head is mounted on a one-axis goniometer and levelled in a way that a distant target (e.i. a 100 W bulb, farther than 200 m) moves on a single line on the image returned by the camera when goniometer angle is changed. The next step consists in finding the prism angles that combined together will not induce image deviation. This will be considered as the centre of the mosaic. From this step begin an iterative process in which the goniometer is indented by few degrees and by a combined motion of the prisms, the distant target is brought back in the centre of the NFOV. The rotation angles of the prisms to reach this point are noted. This process is repeated till the maximum deviation of the prisms. The relation between the deviation angle and prisms angle are noted in a lookup table that will be used at run time to reach a point in the mosaic image space by the prisms. Linear interpolation is used for intermediate value without significant error. A point in the mosaic image space is then viewed as the length of a vector from the centre of the mosaic to this point (that could be found in the lookup table) and a rotation from the

calibration line to the point (see Figure 12). To bring the NFOV in this position, just sum values from the table and the rotation to bring the vector in position.

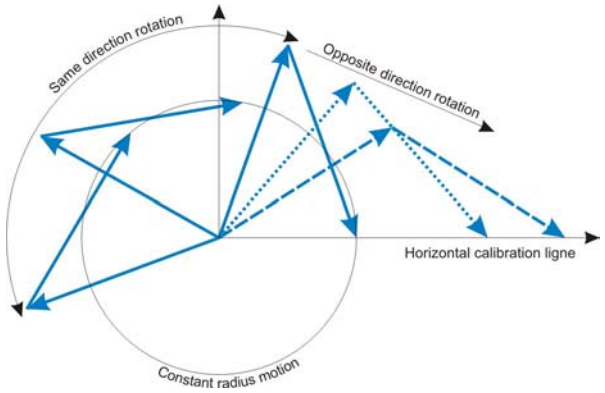

Figure 12: Deviation of the NFOV image VS prisms rotation. If prisms rotate in opposite direction, deviation will be on a radial line. If prisms rotate at same speed in same direction, deviation will be on a constant radius. Combination of motion could bring the NFOV anywhere in the mosaic image space.

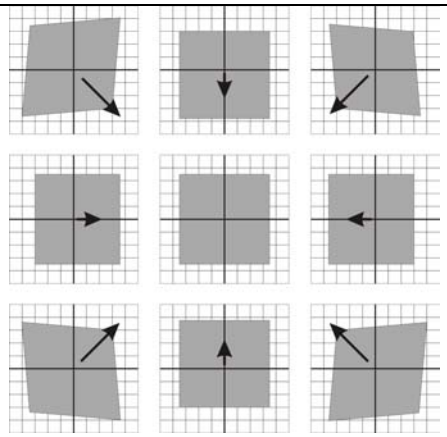

Figure 13: Linear distortion induced by the prisms. The nine grey squares represent the 10° NFOV at their maximal horizontal, vertical and combined deviation positions. Arrows show the amplitude and direction of the linear distortion. Typical distortions measured on the corner images are ~7% in both direction.

6.4 Image Calibration and Distortion Corrections

In the previous section, we have presented the procedure to calibrate NFOV deviation using the prisms. This calibration is sometimes enough to use the system as a general surveillance device to produce good quality imagery. However, if the end usage is aerial imagery, where ground targets should be geo-referenced, another level of calibration is required in order to correct optical distortions and rectify the images. Standard techniques generally found in photogrammetry could be used to obtain intrinsic (and distortion) parameters of the sensor. Matlab add-on and commercial product[1] are currently under study. However, those techniques assume an optical configuration that does not change during the imaging process. In our case, the rotating prisms change significantly the optical configuration and should be taken into consideration (see image 13). To use standard camera calibration process, calibration data must be calculated for each imaging position as shown in image 5. At run time, the corresponding intrinsic parameters will be fetched from a table and used for image correction.

7.0 DISCUSSIONS AND APPLICATION

The step-stare imaging system presented in this paper finds obvious applications in which high-resolution, wide field of view imagery is required and in which camera systems to achieve the task are too big, heavy or simply too expensive to risk loosing them (some UAVs crash, apparently!). One interesting aspect of this concept is that it could be scaled and adapted to almost any kind of IR camera. It becomes thinkable to use small bolometer camera sporting resolution in the 160x120 pixel range with small prisms steering mechanism to provide small tactical UAV with better imaging capability. Such a system could offer

[1] We use PhotoModeler calibration package from EOS Systems inc. Vancouver, Canada. www.photomodeler.com.

800x600 pixel mosaic image every 4 seconds in a package below 3 kg, assuming that the image storage is not on board.

The Risley's prism opto-mechanical pointing device was adapted for multiple IR cameras of different IR bands and has proved itself in numerous flight and ground trials here at DRDC Valcartier. The challenge now will be to miniaturize the system for an optical aperture in the 25 mm range found on micro-bolometer camera and modify the mechanical device in a way to compensate the torque induced on the flying platform by the acceleration of the prisms.

Figure 14: Snapshot of mosaic image created using the step-stare imaging system.

8.0 CONCLUSION

A novel concept of imaging system using an opto-mechanical pointing device based on Risley's prisms has been developed. The step-stare system makes it possible to solve the dichotomy of the need of a wide field of view for detection and high resolution for identification by bringing the detection capability equivalent of the narrow field in the whole large area mosaic image. This technique could eventually provide a small UAV with high-resolution imager that will be lighter, cheaper and more compact. The algorithms developed are general enough to be used with other flight systems (like commercial stabilized "ball") or for ground surveillance. One important factor to evaluate is to what extent positional errors, rotational errors and measurement delays affect the creation of the mosaic and what can be tolerated. If errors are too important, we will have to consider adding features like content-based image registration. Experimentations with the system installed on a rail with carriage mounted on the roof of a building to simulate scaled down flight displacements (6 degrees of freedom) are planned for the months to come.

9.0 ACKNOWLEDGMENTS

Defence R&D Canada (DRDC) and the National Secretariat for Search and Rescue (NSS) sponsor this project. It is a pleasure to acknowledge the work carried out by Mario Pichette, Nicolas Bédard-Maltais and Louis-Philippe Giguère on the setup and control software. Special thanks to Paul Chevrette who has been the instigator of the project and our mentor. Paul is now enjoying a well-deserved retirement.

10.0 REFERENCES

[1] P. Chevrette, B. Ricard and M. Pichette, “Flight Testing the Infrared Eye Prototype”, in *Thermosense XXIV*, Xavier P. Maldague, Andres E. Rozlosnik, *Proc. SPIE Vol.* **4710**, pp. 241-252, 2002.

[2] P. Chevrette and B. Ricard, “Infrared Eye: A human vision based display”, in *Cockpit Displays VI: Displays for Defense Applications*, Darrel G. Hopper, *Proc. SPIE Vol.* **3690**, pp. 94-102, 1999.

[3] V. Lavigne, “Imagerie infrarouge haute résolution par mosaïque d'images géo-référencées", Master's Thesis, Université Laval, Québec, Canada, February 2005.

[4] V. Lavigne, B. Ricard, P. Chevrette and A. Zaccarin, “Step-stare Technique for Airborne, High-Resolution Infrared Imaging”, in *Airborne Intelligence, Surveillance, Reconnaissance (ISR) Systems and Applications*, *Proc. SPIE Vol.* **5409**, Orlando (Kissimmee), Florida, pp. 128-138, 2004.

[5] N. Bowditch, *The American Practical Navigator*, Chap. 22, pp. 340, National Imagery and Mapping Agency, Bethesda, Maryland, US Gov NVPUB9V1, 1995, http://www.irbs.com/bowditch/.